

Article

Response of Liquid Water and Vapor Flow to Rainfall Events in Sandy Soil of Arid and Semi-Arid Regions

Ting Lu ^{1,2,3}, Ce Zheng ^{1,2,3,*} , Bao Zhou ⁴, Jing Wu ^{1,4}, Xueke Wang ¹, Yuan Zhao ¹, Xiuhua Liu ^{1,2,3}  and Wenqian Yuan ⁵

¹ School of Water and Environment, Chang'an University, Xi'an 710054, China

² Key Laboratory of Subsurface Hydrology and Ecological Effect in Arid Region of Ministry of Education, Chang'an University, Xi'an 710054, China

³ Key Laboratory of Eco-Hydrology and Water Security in Arid and Semi-Arid Regions of the Ministry of Water Resources, Chang'an University, Xi'an 710054, China

⁴ Geological Environmental Monitoring Central Station of Qinghai Province, Xining 810008, China

⁵ School of Economics, Xi'an University of Finance and Economics, Xi'an 710100, China

* Correspondence: zhengce@chd.edu.cn

Abstract: In arid and semi-arid regions, rainfall takes on a critical significance to both agricultural and engineering construction activities, and the transport process and driving mechanism of soil water under rainfall conditions are in need of further investigation. To clarify the variations in soil moisture, temperature, and liquid and vapor flux under various rainfall scenarios, the Mu Us Sandy Land was selected as the study region, and a water–vapor–heat transport model was established using the Hydrus-1D software with in situ observed soil and meteorological data. The simulated results were in good agreement with the measured data during both the calibration and validation periods, suggesting that the model was accurate and applicable to the study region. The variations in the selected dry and rainy periods proved the significant effect of rainfall events on soil matric potential, temperature, and driving forces. When rainfall occurred, the hydraulic conductivity for liquid water rose by three to five orders of magnitude, driving the liquid water flow downward. In contrast, the vapor flux played a vital role in soil water movement, accounting for about 15% of the total water flux in the shallow layer when the soil was dry, while it became non-significant during rainy periods due to the reduction in hydraulic conductivity for vapor and the temperature gradient. These results clarified the mechanisms of soil liquid water and vapor movement in arid areas, which could provide scientific support for future studies on vegetation restoration and ecosystem sustainability in ecologically fragile areas.

Keywords: soil water flux; vapor flow; rainfall event; Hydrus-1D model; arid and semi-arid regions



Citation: Lu, T.; Zheng, C.; Zhou, B.; Wu, J.; Wang, X.; Zhao, Y.; Liu, X.; Yuan, W. Response of Liquid Water and Vapor Flow to Rainfall Events in Sandy Soil of Arid and Semi-Arid Regions. *Agronomy* **2023**, *13*, 2424. <https://doi.org/10.3390/agronomy13092424>

Academic Editor: Gianni Bellocchi

Received: 7 August 2023

Revised: 14 September 2023

Accepted: 15 September 2023

Published: 20 September 2023



Copyright: © 2023 by the authors. Licensee MDPI, Basel, Switzerland. This article is an open access article distributed under the terms and conditions of the Creative Commons Attribution (CC BY) license (<https://creativecommons.org/licenses/by/4.0/>).

1. Introduction

Arid and semi-arid regions are extensively distributed around the world, covering over 30% of the Earth's surface, and their proportion continues to expand [1,2]. Affected by strong evaporation and scarce rainfall, the soil is relatively dry and vegetation is sparse, leading to gradual land desertification [3–5]. In these regions, rainfall infiltration has long been regarded as the greatest challenge to the hydrological cycle, which plays a critical role in agricultural activities, as well as affecting soil water distribution [6–8]. Meanwhile, soil water in these dry regions is a limited resource, which is thought to be the primary regulator for land desertification, and is a paramount water source for the growth and transpiration of many plants, especially in areas with a deep groundwater depth [9,10]. Since rainfall-derived soil water is more readily available, studies have proved that plants preferentially utilize soil water over groundwater [11]. Therefore, clarifying the mechanism of soil water movement and its response to rainfall events can provide more insights

into the hydrological cycle in arid and semi-arid regions, which is critical to vegetation restoration and ecosystem sustainability in ecologically fragile areas [12–14].

As the key zone connecting various strata, the vadose zone provides a place for the transmission of soil water and heat, the exchange of water and energy between the environment and soil, and the root water uptake [15–17]. A considerable amount of research has been conducted on the vadose zone, especially regarding the mechanism of rainfall infiltration and soil water movement [8,18]. For instance, Cheng et al. [19] estimated the soil water response to precipitation based on the water balance method in the Mu Us Sandy Land. They proposed that the wetting front for 53.8 and 24.2 mm of accumulative rainfall could penetrate to 200 cm depth when the antecedent soil water contents were approximately 0.065 and 0.102 $\text{cm}^3 \text{cm}^{-3}$, respectively. In dry sand dunes, it was calculated that the wetting front could soon recharge to 100 cm depth after 100 mm of rainfall and reached 140 cm several days later [20]. With the rapid advances in computation technology, numerical simulation has been increasingly used in relevant research. Simulation research using numerical software has become more prevalent because fieldwork is complicated and unpredictable [21,22]. The emergence of relevant software, such as SHAW, Hydrus-1D, CoupModel, and STEMMUS, has significantly improved the convenience of research related to soil water movement (e.g., improved dependability and increased accuracy of predictions) [23–25].

Based on Richard's equation, Philip and de Vries [26] initially developed the theory of coupled liquid and vapor transfer under isothermal conditions. Cass et al. [27] proposed the enhancement factor of vapor flow and estimated it using different calculation methods. Cahill and Parlange [28] quantitatively estimated the effect of vapor flow, suggesting that vapor flux can account for an appreciable 25% of total water flux at the surface. Meanwhile, vapor flux in the upper layer could transport a significant amount (up to 50%) of the overall heat flux. Since then, vapor flow driven by the temperature gradient has been considered an important component of soil water flow, especially in drylands with low soil moisture [18,29–32]. Nevertheless, research on the coupled liquid and vapor flow during various dry and wet conditions is still limited, especially for studies based on in situ experiments rather than laboratory tests [33]. The soil water transport process and its driving factors, including liquid water and vapor water, have not been fully explored under drought and various rainfall conditions.

To gain more insights into these issues, the Mu Us Sandy Land in northwest China was selected as the research object. Through field investigation, in situ and laboratory tests, and numerical simulation, this study attempted to clarify the response of both liquid and vapor flow to rainfall events. The specific research goals of this work were (i) to establish a coupled water, vapor, and heat transport model using Hydrus-1D and verify its accuracy and applicability; (ii) to clarify the distribution and variations in soil moisture, temperature, and water flux before and after rainfall; and (iii) to discuss the impact of various rainfall events on soil water movement and the significance of vapor flux in soil water transfer.

2. Materials and Methods

2.1. Field Tests

2.1.1. Description of the Study Site

The Mu Us Sandy Land, one of the four largest sandy lands in China, covering an area of 42,200 km^2 , is located between the Ordos Plateau and the Loess Plateau of northwestern China, as shown in Figure 1. It is an ecologically fragile zone in the Yellow River basin and one of the focal points of the country's sandstorm defense. Sand is the dominant soil in areas of the Mu Us Sandy Land, and most of the sandy land belongs to the temperate semi-arid region [11,14,25,34].

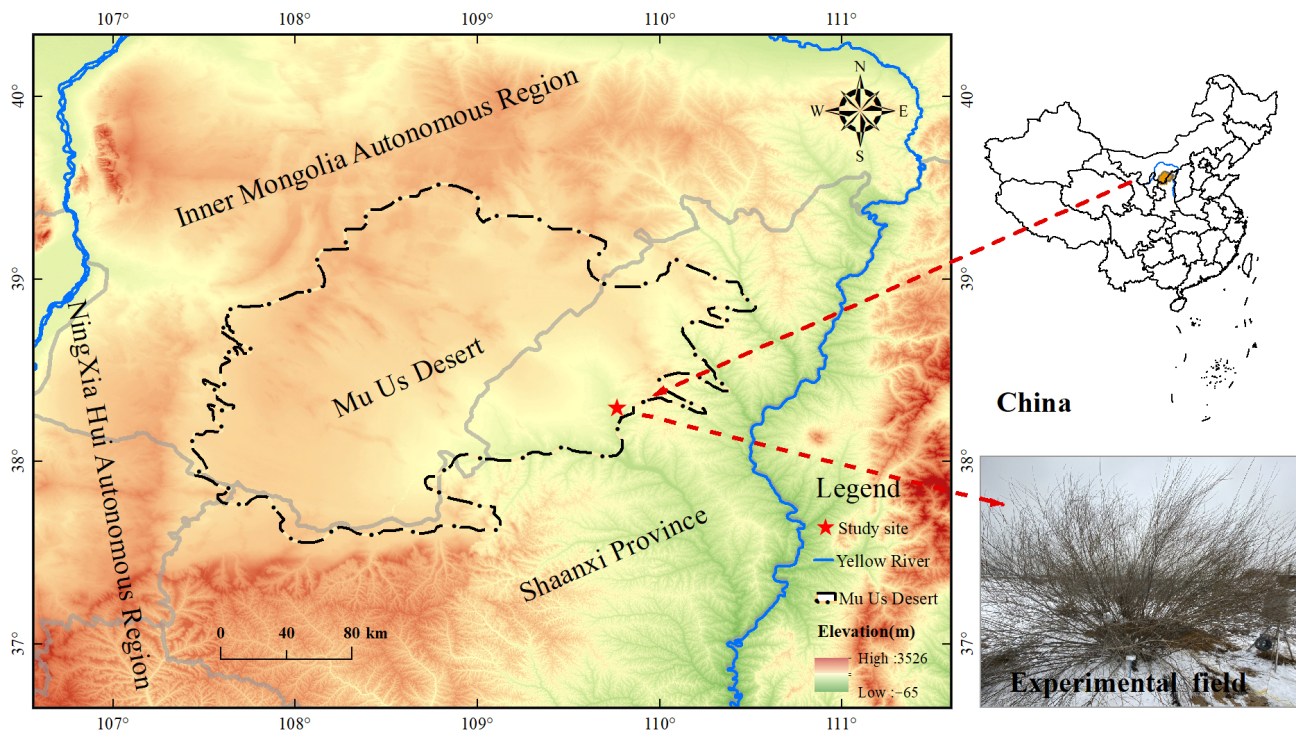


Figure 1. Location and the experiment layout of the study site.

In this study, an in situ observation site was selected in the southeast of the Mu Us Sandy Land (Figure 1, adapted from Chen et al. [14]), located in Yulin Desert Ecological Station of the State Forestry Administration ($38^{\circ}23' \text{ N}$, $109^{\circ}42' \text{ E}$). As indicated by the collected meteorological data since 1961 (from the local weather station), the average yearly temperature is 6.4°C , and the annual evaporation and precipitation are 2343 and 360 mm, respectively. Note the precipitation distribution is uneven, mainly concentrated from July to September, accounting for more than 70% of the total precipitation. The groundwater depth usually fluctuates between 8 and 10 m around the study site.

2.1.2. In Situ Experiments and Observation

At the study site, the soil surface is flat with vegetation covering less than 5%, meaning that the impact of vegetation on soil water transport can be ignored. To obtain soil physical properties, samples at different depths (with a 20 cm interval from the surface to 300 cm depth and a 50 cm interval from 300 cm to 630 cm depth) were collected using the soil drilling method and then investigated in the laboratory to determine their physical properties. According to the soil classification standard of the United States Agriculture Department, sand is the dominating soil [35]. The soil profile was divided into five layers, as listed in Table 1. For determining the soil hydraulic properties, both experimental (including oven-drying and double-ring infiltration tests) and predictive methods were applied. The specific parameter determination processes and adopted values are introduced in the following section.

Subsequently, an observation well (with a diameter of 150 cm) was dug in which to place measuring instruments (as shown in Figure 1). The Hydra Probe II sensors were installed horizontally at 10, 50, 100, 200, 400, and 630 cm depths through the wall of the monitoring well to observe changes in soil temperature and soil moisture. To avoid the influence of the well itself on the observation data, the distance of the sensors from the wellbore exceeded 50 cm, and the observation started 6 months after the installation to allow the soil to establish better contact with the sensors. Before installation, these sensors were calibrated using gravimetric measurements (using the oven-drying method) taken from the same soil horizons. For soil moisture measurements, the principle of the Hydra Probe

II sensors is based on the frequency-domain (FD) method since the permittivity of liquid water (≈ 78) is significantly higher than the other components (e.g., air, soil matrix). Due to their relatively high accuracy, FD sensors are widely applied for field soil water content observation [36,37]. In addition, a micro-meteorology station was also installed at the study site to monitor meteorological variables (i.e., rainfall, air temperature, relative humidity, and wind speed at 2 m above the surface). After installation, the in situ measuring sensors for soil and meteorology were linked to the solar-powered automatic data loggers CR1000 and Em50, respectively, and the observation data were recorded at a 10 min interval.

Table 1. Soil physical analysis in different layers of the study area.

Soil Layer (cm)	Soil Particle Composition			Bulk Density (g cm^{-3})
	Sand (%)	Silt (%)	Clay (%)	
0–80	95.8	3.2	1.0	1.57
80–160	90.1	5.4	4.5	1.51
160–230	91.7	5.2	3.1	1.52
230–560	94.0	4.7	1.3	1.57
560–630	95.4	3.5	1.1	1.57

In this study, the period of 1 April–31 October 2018, was selected for detailed analysis. The reasons for this selection are mainly that approximately 90% of the total rainfall is concentrated from April to October and vegetation growth occurs during this period of the year. Figure 2 presents the variations in the observed meteorological variables during the analyzed period. It can be seen that the precipitation at the test site reached 640.2 mm, far exceeding the local average annual precipitation. The average air temperature, relative humidity, and wind speed during the analyzed period were $17.1\text{ }^{\circ}\text{C}$, 62.6%, and 1.5 m s^{-1} , respectively.

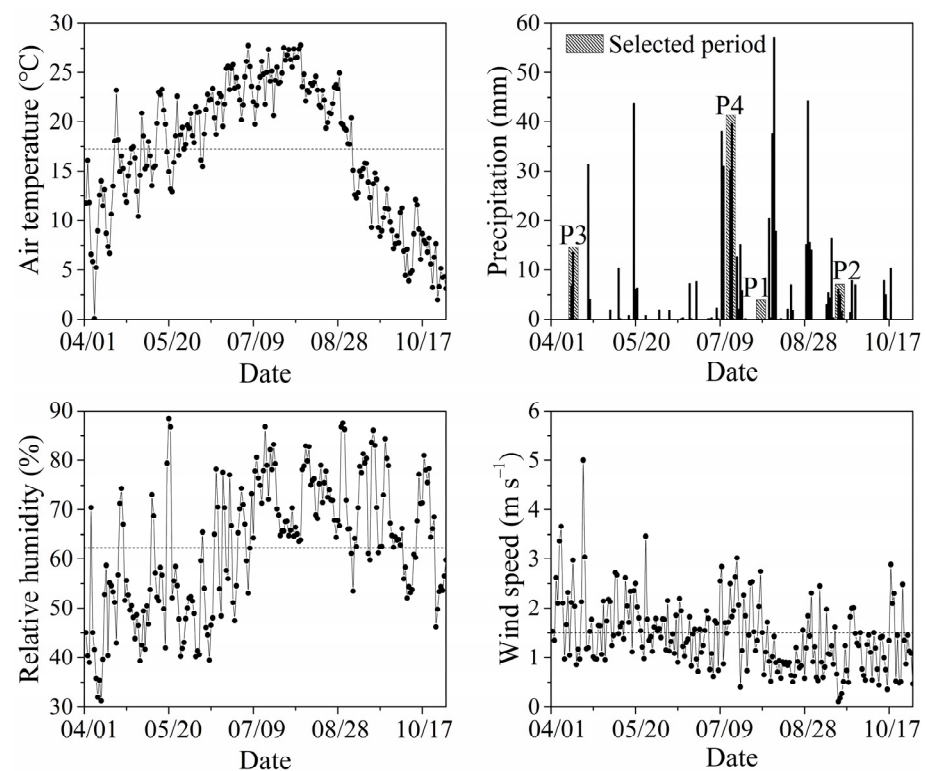


Figure 2. Variations in observed meteorological variables during 1 April–31 October 2018. Note P1, P2, P3, and P4 in the precipitation figure indicate the selected dry, light rainfall, moderate rainfall, and heavy rainfall periods, respectively.

2.2. Model Establishment

2.2.1. Mathematical Equations

For one-dimensional vertical soil water movement, considering the effect of temperature and vapor transport, the governing equation could be expressed using the revised Richard's equation, as indicated below [38,39]:

$$\frac{\partial \theta_l}{\partial t} + \frac{\rho_v}{\rho_l} \frac{\partial \theta_v}{\partial t} = \frac{\partial}{\partial z} \left[K_{lh} \frac{\partial h}{\partial z} + K_{lh} + K_{lT} \frac{\partial T}{\partial z} + K_{vh} \frac{\partial h}{\partial z} + K_{vT} \frac{\partial T}{\partial z} \right] - S \quad (1)$$

where θ_l and θ_v represent the liquid water and vapor content ($\text{cm}^3 \text{cm}^{-3}$), ρ_l and ρ_v represent the density of liquid water and water vapor (g cm^{-3}), t is time (h), z is the spatial coordinate (cm), h is the pressure head (cm), T is temperature (K), K_{lh} and K_{vh} are the isothermal hydraulic conductivities for liquid water and vapor (cm h^{-1}), K_{lT} and K_{vT} are the thermal hydraulic conductivities for liquid water and vapor ($\text{cm}^2 \text{K}^{-1} \text{h}^{-1}$), and S is the sink term accounting for root water uptake (h^{-1}). The conductivities for liquid water and vapor transfer can be expressed as follows:

$$K_{lh} = K_s S_e^l \left[1 - \left(1 - S_e^{1/m} \right)^m \right]^2 \quad K_{lT} = K_{lh} \left(h G_{wt} \frac{1}{\gamma_0} \frac{d\gamma}{dT} \right) \quad (2)$$

$$K_{vh} = \frac{D}{\rho_w} \rho_{sv} H_r \frac{Mg}{RT} \quad K_{vT} = \frac{D}{\rho_w} \eta H_r \frac{d\rho_{sv}}{dT} \quad (3)$$

where K_s is the saturated hydraulic conductivity (cm h^{-1}), S_e is the effective liquid saturation, l and m are empirical parameters as defined by Mualem [40], G_{wt} is the gain factor, γ is the surface tension of soil water (J cm^{-2}), γ_0 is the surface tension at 25°C ($=71.89 \text{ g s}^{-2}$), D is the vapor diffusivity in soil ($\text{cm}^2 \text{h}^{-1}$), ρ_{sv} is the saturated vapor density (g cm^{-3}), H_r is the relative humidity, M is the molecular weight of water ($=0.018015 \text{ kg mol}^{-1}$), g is the gravitational acceleration, R is the universal gas constant ($=8.315 \text{ J mol}^{-1} \text{K}^{-1}$), and η is the enhancement factor. The K_{lh} is calculated using the van Genuchten model as follows [41]:

$$\theta_l = \begin{cases} \theta_r + \frac{\theta_s - \theta_r}{[1 + |\alpha h|^n]^m} & h < 0 \\ \theta_s & h \geq 0 \end{cases} \quad (4)$$

where θ_r and θ_s are the residual and saturated water contents ($\text{cm}^3 \text{cm}^{-3}$), respectively, α (cm^{-1}) and n are empirical parameters.

To determine the soil hydraulic properties at the study site, the oven-drying and the double-ring infiltration methods were utilized to measure saturated water content (θ_s) and the saturated hydraulic conductivity (K_s), while the values of other parameters (including θ_r , a , and n) of the van Genuchten model were obtained using the neural network method with the Rosetta module. This module is directly implemented in the Hydrus-1D program, and estimates hydraulic parameters according to the measured data of soil particle composition and bulk density (as listed in Table 1) [35]. Subsequently, to obtain simulation results with better fitting accuracy, the Levenberg–Marquardt algorithm, which is also directly implemented into the inverse module of Hydrus-1D, is used to optimize these parameters using the observed soil water content data [42]. The estimation process is as follows:

$$\phi_s = \sum_{i=1}^{m_q} [p_m(z, t) - p_s(z, t)]^2 \quad (5)$$

where ϕ_s is the cumulative error between measured and simulated values, $p_m(z, t)$ and $p_s(z, t)$ are the measured and simulated soil water content at depth z at time t , respectively, and m_q represents the number of data used for the inverse. As indicated by Equation (5), this method is based upon the minimization of the discrepancy between the observed values and simulated water content at selected depths. According to a parameter sensitivity

analysis, the empirical parameters α and n have a significant impact on the simulation results. Therefore, these two parameters were mainly identified during the optimization process. The optimized parameters for numerical simulation at different soil layers are listed in Table 2.

Table 2. Optimized soil hydraulic parameters of different layers.

Soil Layer (cm)	$\theta_r/(\text{cm}^3 \text{ cm}^{-3})$	$\theta_s/(\text{cm}^3 \text{ cm}^{-3})$	$\alpha/(\text{cm}^{-1})$	$n/(-)$	$K_s/(\text{cm h}^{-1})$	$l/(-)$
0–80	0.008	0.375	0.027	1.57	57	0.5
80–160	0.015	0.427	0.028	1.51	34	0.5
160–230	0.011	0.415	0.029	1.64	50	0.5
230–560	0.010	0.402	0.021	1.87	51	0.5
560–630	0.011	0.380	0.023	1.76	53	0.5

On the other hand, considering the effect of temperature and vapor flow, the governing equation for vertical soil heat flow in the vadose zone could be expressed using the energy conservation equation, as indicated below [38,39]:

$$\frac{\partial C_p T}{\partial t} + L_0 \frac{\partial \theta_v}{\partial t} = \frac{\partial}{\partial z} \left[\lambda(\theta_l) \frac{\partial T}{\partial z} \right] - C_w \frac{\partial q_l T}{\partial z} - C_v \frac{\partial q_v T}{\partial z} - L_0 \frac{\partial q_v}{\partial z} - C_w S T \quad (6)$$

where C_p , C_w , and C_v are the volumetric heat capacities of moist soil, liquid water and vapor phase ($\text{J cm}^{-3} \text{ K}^{-1}$), respectively. L_0 is the latent heat of vaporization of liquid water (J cm^{-3}), q_l and q_v are the flux density of liquid water and vapor (cm h^{-1}), and λ is the thermal conductivity of soil ($\text{J cm}^{-1} \text{ h}^{-1} \text{ K}^{-1}$), which can be estimated using the Chung and Horton equation [43]:

$$\lambda(\theta_l) = b_1 + b_2 \theta_l + b_3 \theta_l^{0.5} \quad (7)$$

where b_1 , b_2 , and b_3 represent empirical factors that reflect soil texture, which are defined in the Hydrus-1D program and used in the established model as 0.228, -2.406 , and $4.909 \text{ W m}^{-1} \text{ K}^{-1}$ for sands, respectively.

Since the vegetation is quite sparse at the study site, covering less than 5% of the soil surface, the effect of root water uptake for water flow and heat transport is not considered in the simulation process. Detailed calculations for the above-mentioned soil hydraulic and thermal parameters can be found in Zheng et al. [25] and Saito et al. [38].

2.2.2. Establishment of Hydrus-1D Model

Due to its convenient operation and comprehensive functions, research on soil water movement has made substantial use of the Hydrus-1D program [44,45]. On the basis of soil water transport research, Scanlon et al. [17] firstly considered vapor flow and its phase-transition effects in Hydrus-1D modeling research. Then, Saito et al. [38] took surface water and thermal equilibrium procedures into account in the Hydrus-1D code, and improved the flexibility of setting meteorological conditions in the model. Since then, the standard Hydrus-1D model could be utilized to investigate the coupled water–vapor–heat transport process.

By collecting the in situ monitoring soil and meteorological data, a model for the combined transfer of liquid water, water vapor, and heat established using the Hydrus-1D software is used to obtain the liquid water and vapor flux. To gain detailed diurnal variations, the unit of the simulation period was hours (h) with a total time of 5136 h and 2184 h for the calibration (1 April–31 October 2018) and validation (1 April–30 June 2019) periods, respectively. Moreover, spatial discretization was carried out at an interval of 2 cm from the surface to 630 cm below, with a total of 316 nodes. For the initial water and heat conditions of the model (Equation (8)), the water content and temperature data observed on 1 April at depths of 10, 50, 100, 200, 400, and 630 were used for linear interpolation to obtain the initial conditions of the 0–630 cm soil profile. As indicated in

Equations (9) and (10), the upper boundary for water flow is controlled by meteorological factors and determined by rainfall and evaporation conditions, and free drainage is the lower boundary condition because it is far from the groundwater level (nearly 10 m). For soil heat transport, the calculated surface temperature (using soil temperature data observed in the shallow layer [46]) and measured bottom temperature (from the Hydra Probe II sensor located at 630 cm) values are employed as the circumstances at the upper and lower boundaries, respectively (Equation (11)).

$$\theta_l(z, t) = \theta_{l,i}(z) \quad T(z, t) = T_i(z) \quad t = 0 \quad (8)$$

$$\left| -K_{lh} \frac{\partial h}{\partial z} - K_{lh} - K_{lT} \frac{\partial T}{\partial z} - K_{vh} \frac{\partial h}{\partial z} - K_{vT} \frac{\partial T}{\partial z} \right| \leq E_m \quad z = 0 \quad (9)$$

$$\frac{\partial h(z, t)}{\partial z} \quad z = 630 \text{ cm} \quad (10)$$

$$T(z, t) = T_0(t) \quad z = 0 \text{ or } z = 630 \text{ cm} \quad (11)$$

where E_m is the maximum infiltration or evaporation rate at the current moment (cm h^{-1}). For the atmospheric boundary condition, the variation in rainfall was automatically monitored, while hourly potential evaporation (E_p) was estimated as follows:

$$E_p = \frac{\rho_{vs} - \rho_{va}}{r_v + r_s} \quad (12)$$

where ρ_{vs} and ρ_{va} are vapor densities (g cm^{-3}) at the soil surface and the 20 cm height (where the air temperature is measured), respectively, and r_v and r_s are the aerodynamic and soil surface resistances (h cm^{-1}) for vapor movement, respectively. These parameters can be estimated using the observed soil water content and meteorological data, as introduced by Bittelli et al. [31] and Kroener et al. [47]. The calculated values of E_p were in close agreement with the observed data at the Yulin meteorological station.

The main program unit of the Hydrus-1D graphical user interface defines the overall computational environment of the system, containing a project manager and both the pre-processing and post-processing units. The pre-processing unit includes specification of all necessary parameters (as mentioned above) to successfully run the Hydrus-1D FORTRAN codes. The established coupled water–vapor–heat transport model could be utilized to investigate the distribution and variations in soil moisture, temperature, and water flux before and after rainfall.

3. Results

3.1. Model Evaluation and Selection of Analyzed Periods

3.1.1. Model Evaluation

To evaluate the model's accuracy, the measured soil water content and temperature data at depths of 10, 50, 100, 200, 400, and 630 cm during 1 April–31 October 2018 and 1 April–30 June 2019 were used for model calibration and validation, respectively. In addition, mean absolute error (MAE) and root mean square error (RMSE) were the two statistical indicators employed to assess the model's accuracy for describing soil water content and temperature variations.

The observed and simulated soil water contents and temperatures at the research site over the calibration period are compared in Figure 3. The simulated results accurately captured the ups and downs of real soil water content change. Since the middle and bottom soil layers were less affected by external environmental factors, the fitting results of the soil water content were relatively good (e.g., RMSE = 0.005 and 0.002 $\text{cm}^3 \text{cm}^{-3}$ at 200 and 400 cm depths, respectively). Considering the major impact of outside environmental influences, such as strong precipitation and evaporation, the fitting results for the shallow soil water content were relatively poor (e.g., MAE = 0.011 $\text{cm}^3 \text{cm}^{-3}$ and

RMSE = $0.017 \text{ cm}^3 \text{ cm}^{-3}$ at 10 cm depth), whereas the error was within an acceptable range. On the other hand, it could be found that soil temperature during the analyzed period first increased and then decreased as a result of the impact of changing air temperature. Compared with its soil water content simulation results, the fitted soil temperature matched very well with the measured data, with calculated MAE and RMSE values less than $1 \text{ }^\circ\text{C}$ for most depths.

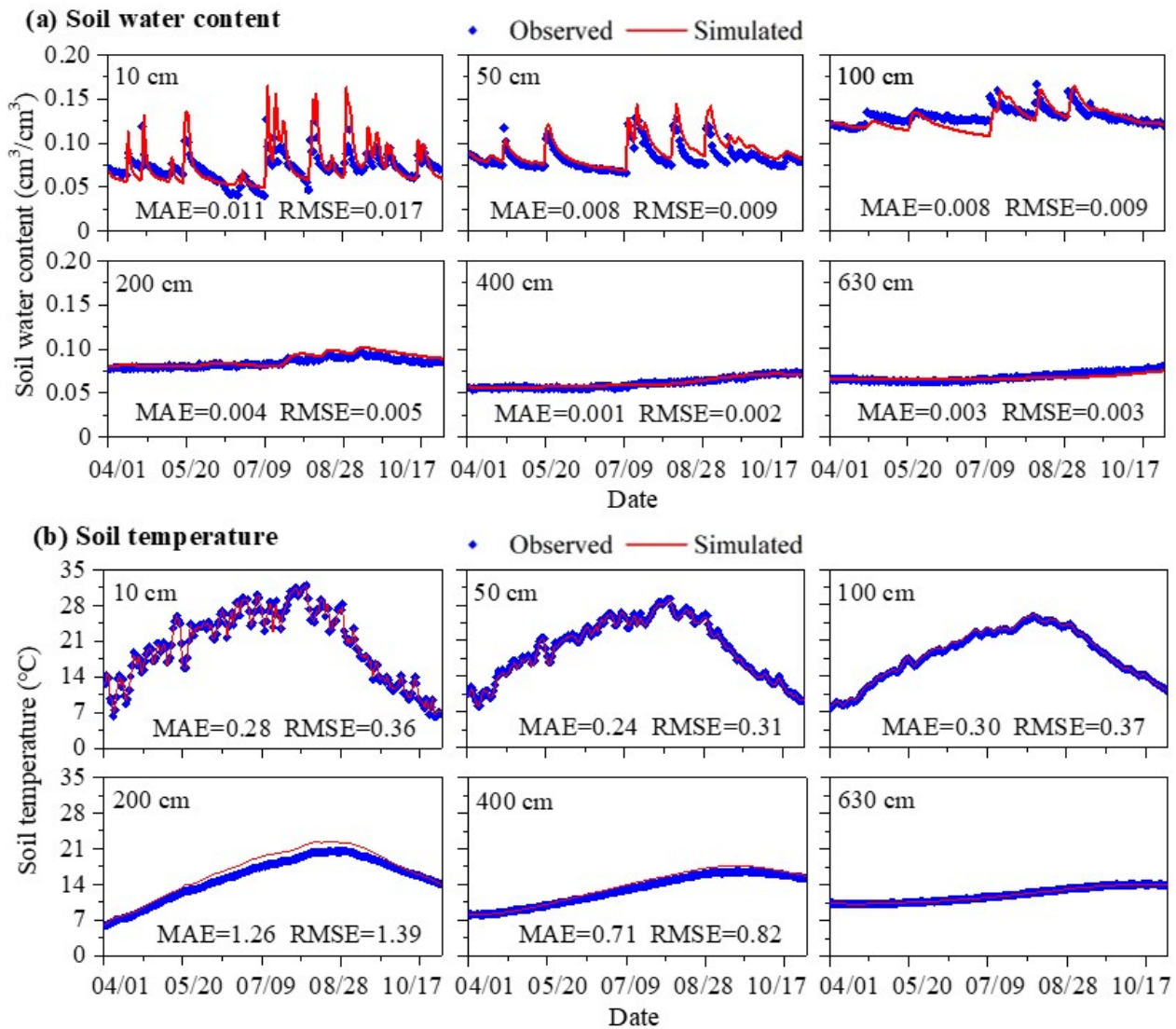


Figure 3. Comparison of simulated and measured soil water content and temperature during the calibration period (1 April–31 October 2018). The units of MAE and RMSE for soil water content and temperature are $\text{cm}^3 \text{ cm}^{-3}$ and $^\circ\text{C}$, respectively.

In addition, the simulated variations were in good agreement with the observed data during the validation period as well (as shown in Figure 4), with the average RMSE values of $0.017 \text{ cm}^3 \text{ cm}^{-3}$ and $1 \text{ }^\circ\text{C}$ for soil water content and temperature, respectively. Taken together, the established model is proved to have high accuracy overall, which suggests that it can be utilized to analyze the coupled liquid water, water vapor, and heat transport inside the arid areas of Mu Us Sandy Land.

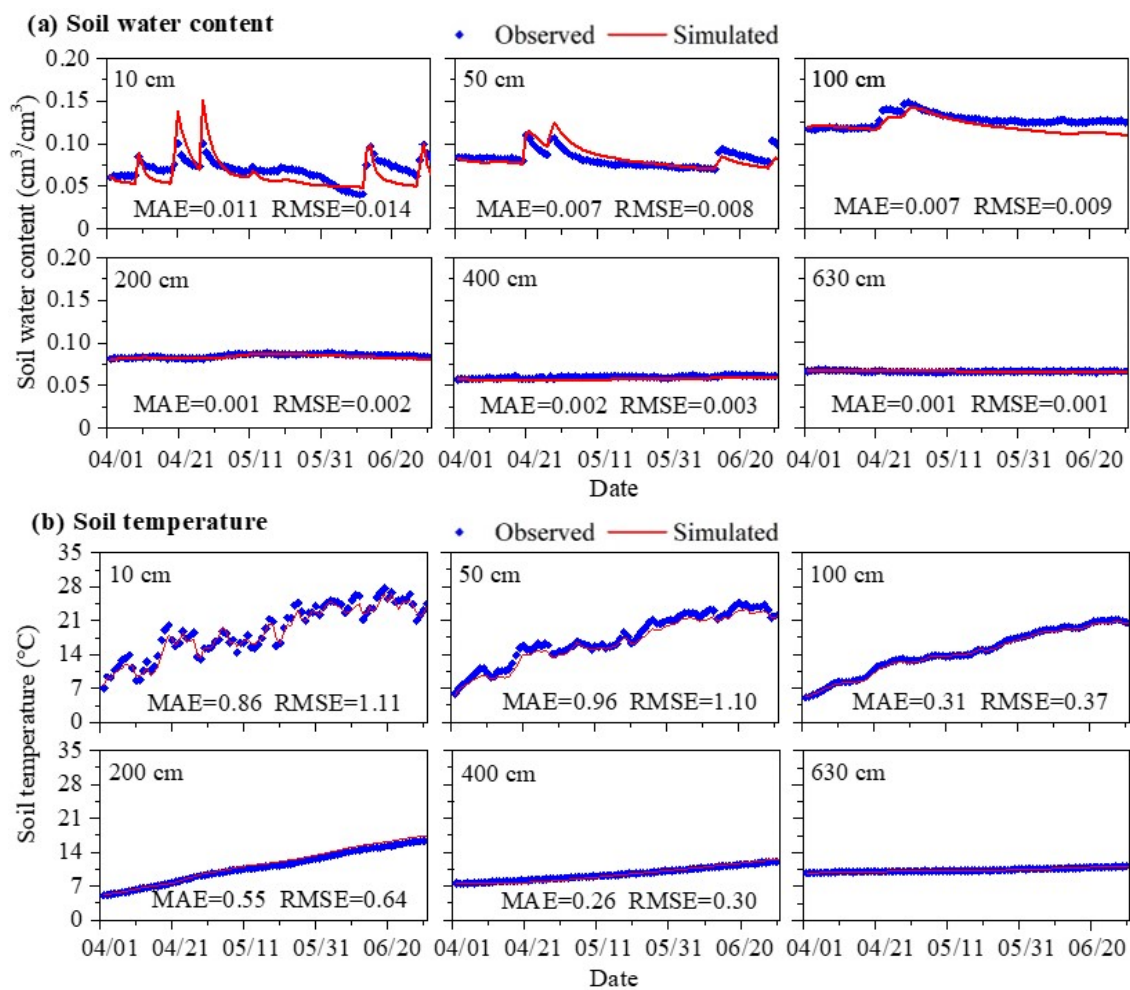


Figure 4. Comparison of simulated and measured soil water content and temperature during the validation period (1 April–30 June 2019). The units of MAE and RMSE for soil water content and temperature are $\text{cm}^3 \text{cm}^{-3}$ and $^{\circ}\text{C}$, respectively.

3.1.2. Selection of Simulation Periods

By collecting the measured precipitation data during the calibration period, the statistical information of the specific daily rainfall amount was sorted, as indicated in Table 3. It is evident that the rainfall amount of 25–50 mm occupies the greatest proportion of the total rainfall amount, followed by the amounts of 10–25 mm and less than 10 mm. To investigate the response of soil hydrothermal and water flux to scenarios with different amounts of rainfall in detail, 5 day short periods with the above-mentioned rainfall scenarios were selected. The selected periods should be as unaffected as possible by previous rainfall, with the soil in a relatively dry state (with the soil water content in the shallow layer less than $0.05 \text{ cm}^3 \text{ cm}^{-3}$) at the beginning of each period. Meanwhile, a drought period (no rainfall for more than 10 days) was selected for comparison. Detailed information for the selected periods is listed in Table 4.

In the following sections, the characteristics of the distribution and variation in soil water content, temperature, driving force for water movement, and liquid and vapor flux under non-isothermal conditions on an hourly scale were specifically analyzed. Note that the influence of rainfall was mainly concentrated in the upper section of the unsaturated zone, but not notable for the lower part. Meanwhile, Figure 2 indicates that during the simulation period, meteorological factors mainly affect the soil moisture and temperature at the soil profile of 0–200 cm, with little impact on soil moisture and temperature below

200 cm. Therefore, the following detailed analysis focused on the layer from the surface to 200 cm soil depth.

Table 3. Characteristics of rainfall distribution during the simulation periods.

Single Rainfall Amount	Times	Total Rainfall Amount (mm)	Proportion in the Total Rainfall Amount
<10 mm	32	125	19.5%
10–25 mm	11	161.8	25.3%
25–50 mm	8	296.2	46.3%
>50 mm	1	57.2	8.9%

Table 4. Detailed information for selected periods.

Period	Date (mm/dd)	Total Rainfall Amount (mm)	Rainfall Distribution for 5 Days (mm)				
			Day 1	Day 2	Day 3	Day 4	Day 5
P1: Dry period	08/01–08/05	0	0	0	0	0	0
P2: Light rainfall period	09/16–09/20	12.8	0	6	5	1.6	0.2
P3: Moderate rainfall period	04/11–04/15	20.4	0	6.8	13.6	0	0
P4: Heavy rainfall period	07/14–07/18	69.8	0	30.2	39.6	0	0

3.2. Spatial and Temporal Distribution of Soil Matric Potential and Its Gradients

3.2.1. Soil Matric Potential

In the selected four periods, the spatial and temporal distributions of the soil matric potential in the profile are depicted in Figure 5. Influenced by evaporation throughout the dry period, the shallow soil's matric potential (mainly for the top 10 cm layer) was obviously lower than that of other soil layers, with a value of $-10,000$ cm (which was set as the minimum value in the Hydrus-1D model). To clarify the distribution characteristics at various levels of the profile, the minimum value in the figure was set to -1000 cm. As depicted in Figure 5, there were two significant characteristics of the matric potential distribution.

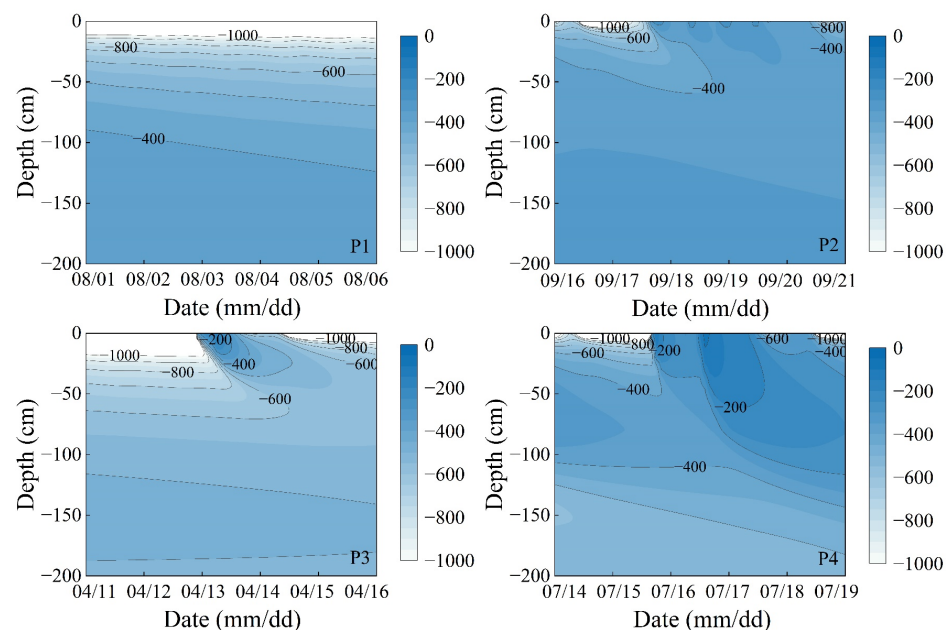


Figure 5. Spatial–temporal distribution of soil matric potential (cm) simulated by the Hydrus-1D model during different periods: P1 (dry period), P2 (light rainfall period), P3 (moderate rainfall period), and P4 (heavy rainfall period).

First, the distribution of the matric potential in the profile during dry and wet days was completely different. In P1, the soil maintained a dry state, and the surface's matric potential decreased to its lowest level. Below the top layers, the matric potential tended to decrease due to the increasing dryness intensity (e.g., decreasing from -1058 cm to -1180 cm at 10 cm). When rainfall occurred, the matric potential distribution in the profile changed significantly. The matric potential of shallow soil increased instantaneously, and the isolines at the depths of 0–50 cm became very dense, with the maximum values reaching -250 , -135 , and -79 cm, respectively, for P2, P3, and P4. Secondly, different rainfall intensities have different effects on matric potential changes (such as infiltration duration and depth). For instance, in P3, since it only rained on the second and third days, the soil on the surface gradually dried out after the rainfall, and the matric potential decreased significantly due to the influence of water infiltration and evaporation. As for P4, the rainfall intensity was relatively high on the second and third days (Table 4), resulting in the matric potential in the profile changing over a wide range. Comparing the results at 100 cm, the matric potential in P4 increased from -370 cm before rainfall to -267 cm at the end of this period, while the matric potential slightly decreased in P2 and P3, reflecting the influence of different rainfall intensities on infiltration depth.

3.2.2. Soil Matric Potential Gradient

Figure 6 presents the spatial and temporal distribution of the soil matric potential gradient in the profile. To be specific, the positive values in the figure indicate that the gradient direction ascended while the negative values indicate the opposite result. Likewise, in order to show the distribution characteristics more clearly, the maximum gradient value in the dry period was located at 40 cm cm^{-1} in the figure.

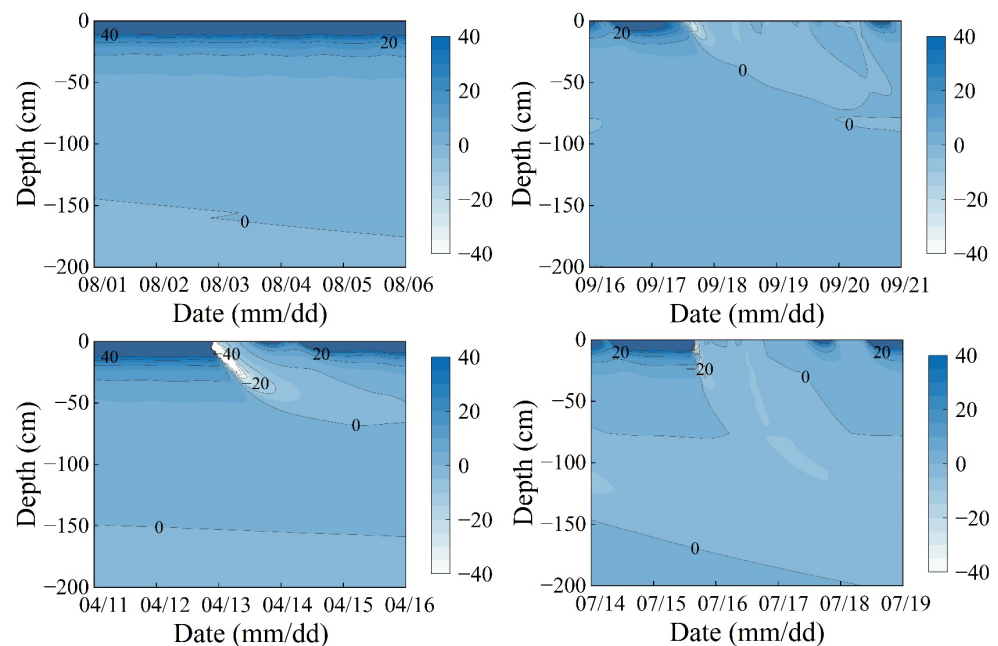


Figure 6. Spatial–temporal distribution of matric potential gradients (cm cm^{-1}) simulated by the Hydrus-1D model during different periods: P1 (dry period), P2 (light rainfall period), P3 (moderate rainfall period), and P4 (heavy rainfall period).

With increasing depth, the gradient of the matric potential decreases significantly. For example, at the beginning of P1, the matric potential gradients at 10, 20, 50, and 100 cm are 48.3 , 16.5 , 3.9 , and 1.2 cm cm^{-1} , respectively. The decrease in the gradient reflects the reduction in the driving force. There exists a divergent zero-gradient plane around 140–180 cm depth, suggesting that the layer has a relatively high matric potential. Since there was no rainfall in P1, the soil gradually dried, leading to a gradual decline in the

zero-gradient plane. Similar to Figure 5, the effect of different rainfall intensities on the matric potential distribution is notable, e.g., the maximum downward gradient value reached -43.8 cm cm^{-1} in P4. During the rainy period, a convergent zero-gradient plane was also identified, which continuously migrated downward from the surface. When the rainfall stopped, a divergent zero-gradient plane reappeared in the shallow layer due to soil evaporation.

3.3. Spatial and Temporal Distribution of Soil Temperature and Its Gradients

3.3.1. Soil Temperature

For the selected four typical periods, the profile's spatial and temporal distributions of soil temperature are shown in Figure 7.

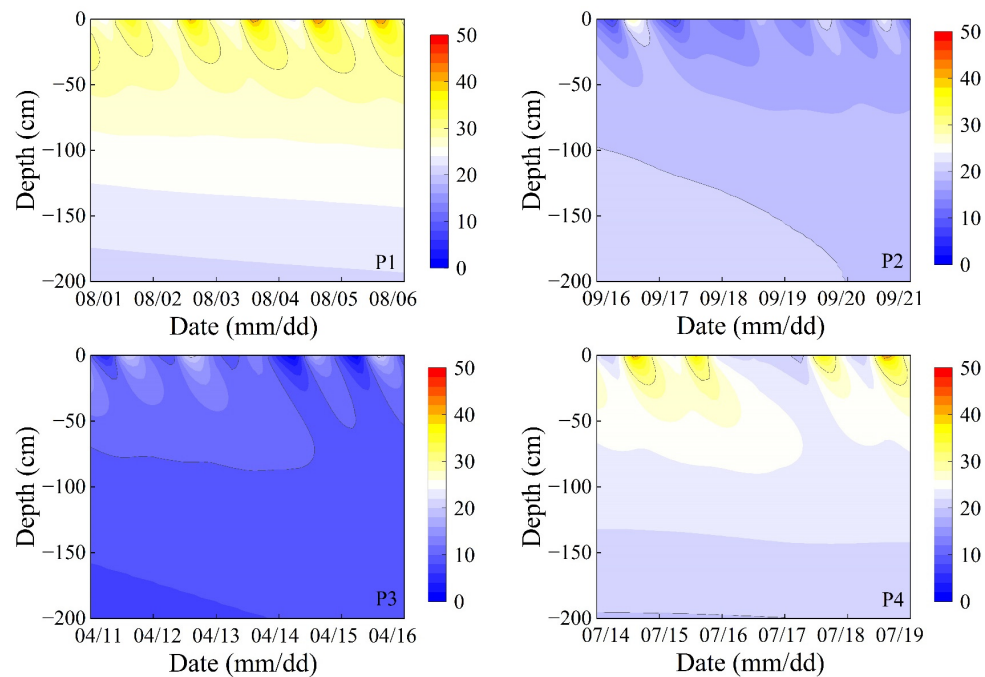


Figure 7. Spatial–temporal distribution of soil temperature ($^{\circ}\text{C}$) simulated by the Hydrus-1D model during different periods: P1 (dry period), P2 (light rainfall period), P3 (moderate rainfall period), and P4 (heavy rainfall period).

Influenced by the air temperature, there was a significant diurnal temperature change in the soil above the shallow 50 cm soil layer, while the changes in soil temperature were relatively smaller in deep layers. Taking period 1 as an example, the surface temperature changed periodically, ranging from 23.3°C to 41.7°C , while the soil temperature at 100 cm increased from 25.2°C to 25.9°C with a variation of only 0.7°C . When it started to rain, the amplitude of the soil temperature change significantly decreased. For instance, in P4, the variation in the surface temperature reached 15.7°C when it did not rain on the first day, while during the following two rainy days, the surface temperature only showed a gradually decreasing trend.

The soil temperature distribution in different periods was also significantly influenced by seasonal changes in air temperature. Deep soil layers' temperatures for P2 were higher than those of shallow soil, which was not consistent with the other three periods. The major reason for the above result was that the vadose zone began to release heat with the decrease in air temperature, causing a gradual decline in temperature in the shallow soil layer.

3.3.2. Soil Temperature Gradient

The soil temperature gradients across time and space in the profile are presented in Figure 8. Similar to the temperature distribution, the gradient of temperature within the

shallow layer also indicated obvious diurnal changes, and the changes were significantly weakened when rainfall occurred.

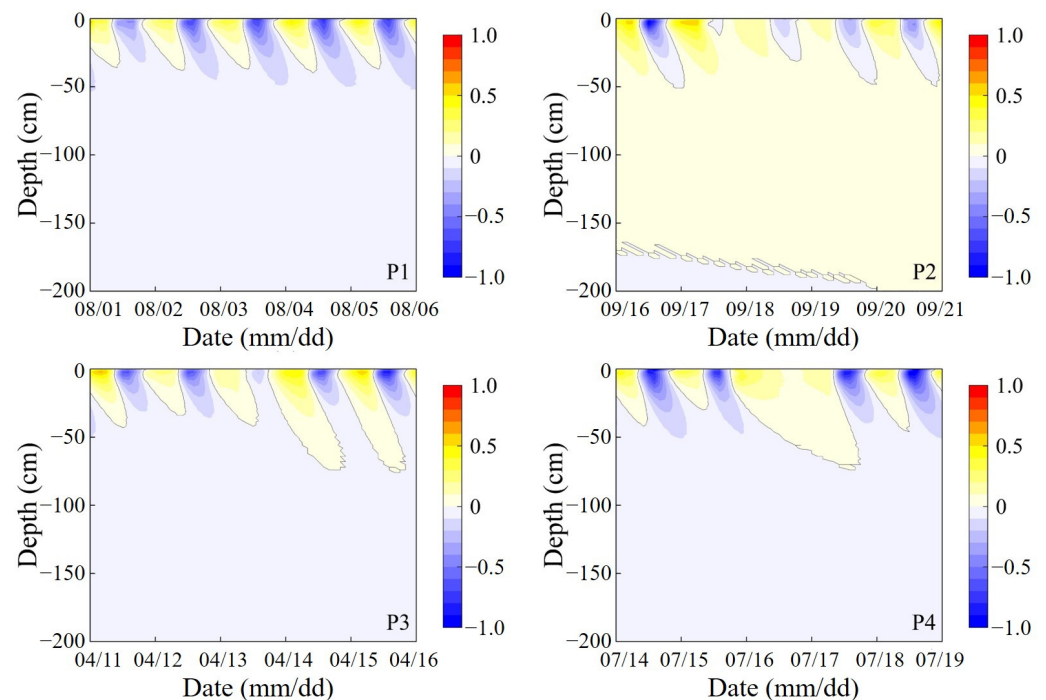


Figure 8. Spatial–temporal distribution of temperature gradients ($^{\circ}\text{C cm}^{-1}$) simulated by the Hydrus-1D model during different periods: P1 (dry period), P2 (light rainfall period), P3 (moderate rainfall period), and P4 (heavy rainfall period).

There were two main zero-gradient planes in the profile. The first one was the divergent plane, which mainly appeared at night. Since the soil temperature of the shallow layer was lower at night, the gradient beyond this plane was positive. The second one was the convergent plane, which mainly exists in the daytime. On that basis, in response to the increase in surface temperature, there was a negative temperature gradient in the shallow layer. Driven by the temperature gradient, both the flux density and transfer direction of liquid water and vapor flow showed significant diurnal variations, which are elucidated in the following section. With the increase in soil depth, the temperature gradient decreased rapidly. It was usually smaller than $0.05\text{ }^{\circ}\text{C cm}^{-1}$ below 100 cm depth, resulting in a decrease in the driving force for liquid and vapor flow.

3.4. Characteristics of Soil Liquid and Vapor Flux

3.4.1. Isothermal Flux

The variations in isothermal liquid (q_{lh}) and vapor (q_{vh}) fluxes driven by the soil water potential gradient during the selected periods are depicted in Figures 9 and 10, respectively, and 2 cm (shallow part), 10 cm (upper part), 50 cm (middle part), and 150 cm (lower part) depths in the profile were employed as representative depths for specific analysis.

It is evident that as the depth increased, the flux drastically dropped, which was largely attributed to the reduction in the soil matric potential and temperature gradients. For q_{lh} , there were obvious daily variations in the shallow layer stratum on dry days, and its values in the upper 100 cm soil layer were all positive, indicating that liquid water flowed upward affected by evaporation. When rainfall occurred, the flux became downward, and the flux showed a downward trend density that varied due to different rainfall events. For instance, the maximum values at 2 cm reached -0.087 , -0.319 and -0.897 cm h^{-1} for P2, P3, and P4, respectively, revealing the instantaneous rainfall intensity.

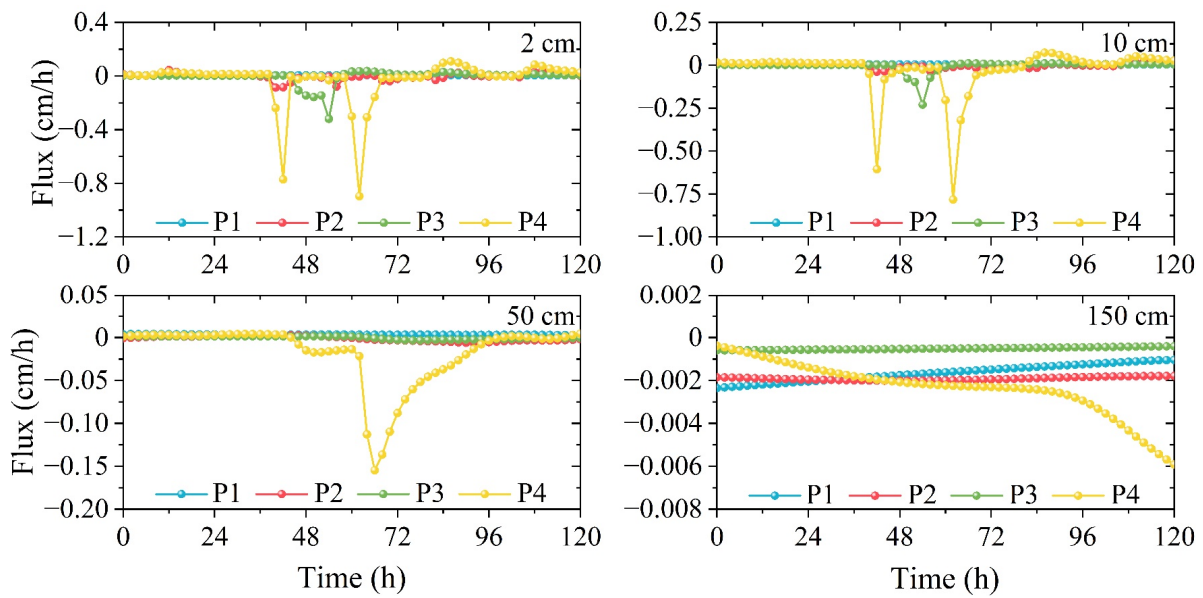


Figure 9. Diurnal variations in the isothermal liquid flux simulated by the Hydrus-1D model at different depths.

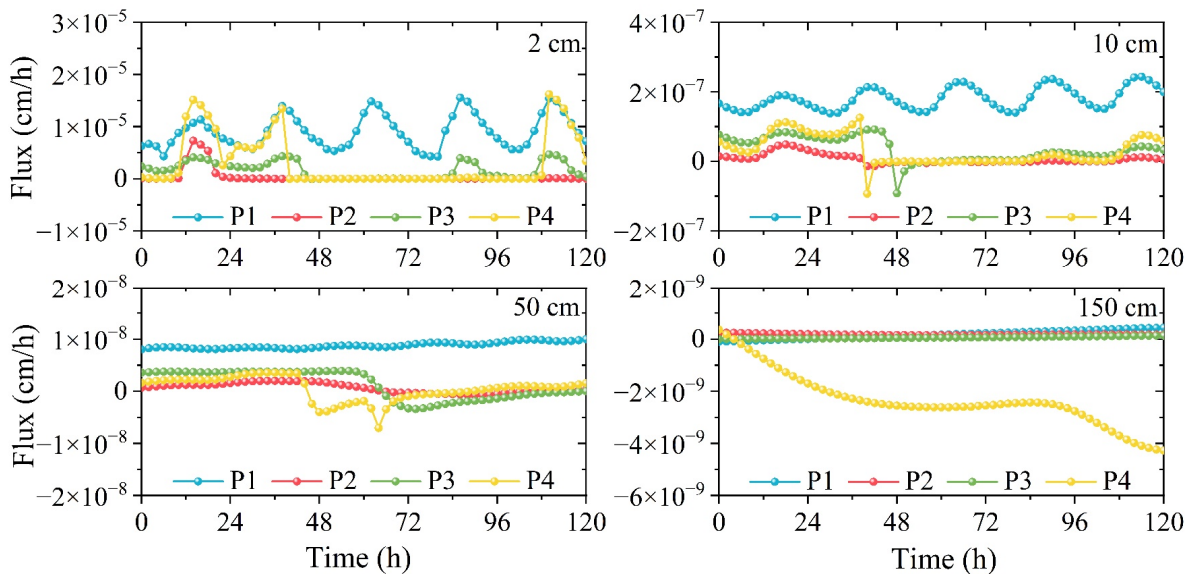


Figure 10. Diurnal variations in the isothermal vapor flux simulated by the Hydrus-1D model at different depths.

The q_{vh} flux was significantly less than q_{lh} , e.g., usually four and seven orders of magnitude smaller in the profile’s top and lower portions, respectively. The maximum value of q_{vh} was only $1.5 \times 10^{-5} \text{ cm h}^{-1}$ in the whole selected period, exerting a very limited effect on the total water flux. This suggests that the vapor flux driven by the matric potential gradient can be ignored.

3.4.2. Thermal Flux

Under the influence of the temperature gradient, there were variations in thermal liquid (q_{lT}) as well as vapor (q_{vT}) fluxes at different depths, indicated in Figures 11 and 12, respectively.

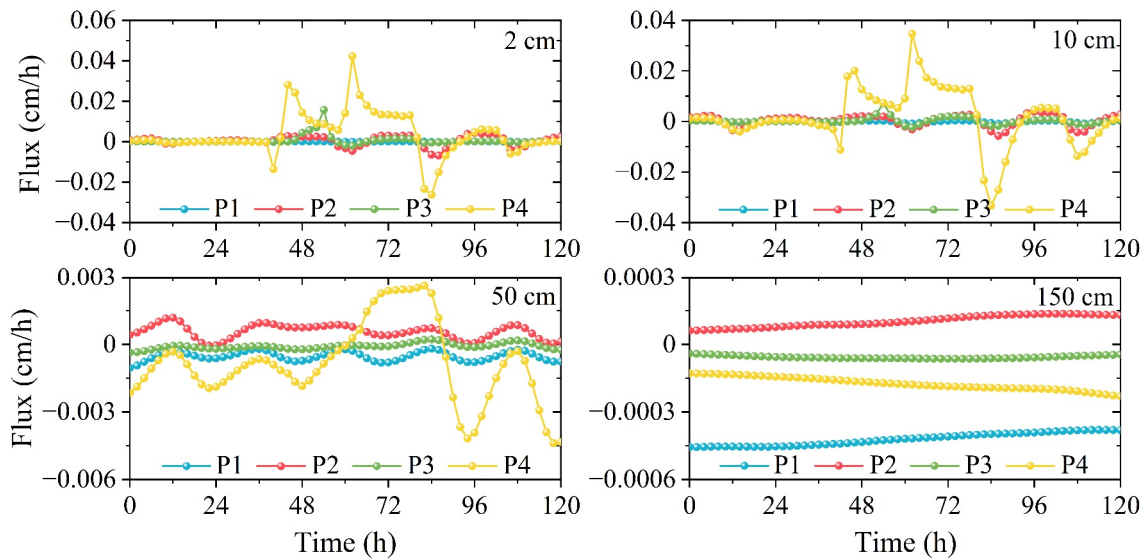


Figure 11. Diurnal variations in the thermal liquid flux simulated by the Hydrus-1D model at different depths.

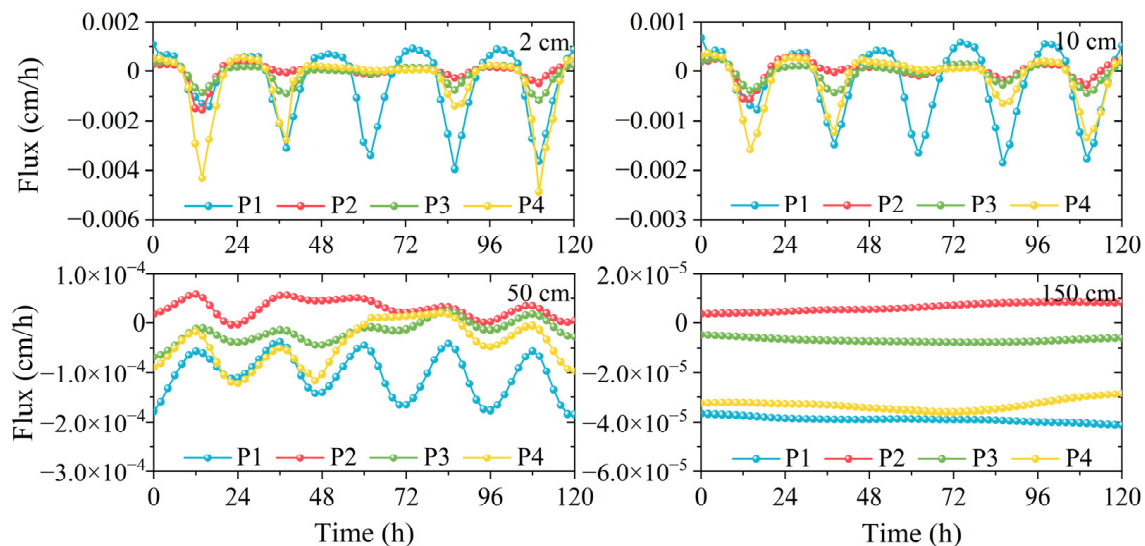


Figure 12. Diurnal variations in the thermal vapor flux simulated by the Hydrus-1D model at different depths.

During the dry period, the q_{vT} flux in the top soil layer was greater than q_{lT} , and both fluxes showed regular daily variations. With the increase in solar radiation in the daytime, the shallow temperature reduced significantly, and the downward flux value was relatively larger in comparison. The maximum q_{vT} flux at 2 cm appeared at 14:00 daily, reaching -0.04 cm h^{-1} . In this condition, the q_{vT} flux maintained was of the same order of magnitude as the q_{lT} flux, reflecting that q_{vT} was a significant part of the total water flux during dry periods.

After being affected by rainfall events, the changing trends in q_{vT} and q_{lT} were completely different. The q_{vT} value in the shallow layer decreased significantly, which was mainly because the increase in water content reduced the hydraulic conductivity of the vapor. At this time, the influence of the vapor flux can be ignored. On the contrary, q_{lT} significantly increased, and its value became much higher than the vapor flux. For example, the maximum value in P4 at the 2 cm depth reached 0.043 cm h^{-1} , while it was only $8.7 \times 10^{-4} \text{ cm h}^{-1}$ in dry conditions.

3.5. Migration of Wetting Front under Different Rainfall Events

Comparing the simulation results of different periods, the impact of rainfall on soil water transfer differed significantly, and the migration of the wetting front could be used to describe the infiltration process. As depicted in Figures 5 and 6, the migration rate of the wetting front significantly changed under different rainfall intensities. For example, in P2, due to the relatively low rainfall intensity, the wetting front only moved to 28 cm at 46 h (10 h after the beginning of rainfall). The infiltration rate tended to decrease, and the wetting front stopped and began to fall at 100 h (located at 74 cm). On the contrary, the wetting front of P4 migrated to 68 cm at 50 h (10 h after the beginning of rainfall), and it eventually exceeded 200 cm.

To quantitatively describe the characteristics of the wetting front, Table 5 lists the calculation results for the infiltration rate and cumulative infiltration amount at different depths, in which the cumulative infiltration amount only considered the downward flux at this depth. With the increase in depth, there was a discernible declining trend in both the maximum infiltration rate and the cumulative amount. The average correlation coefficients of the maximum infiltration rate and the cumulative amount calculated during these three periods were 0.92 and -0.97 , respectively, suggesting that these two variables exhibited significant variation with increasing depth. The reason for the decrease could mainly be attributed to the following two reasons. On one hand, some infiltration water was retained in the upper soil layer after redistribution, increasing the soil moisture there. Then, the evaporation process would dry the wetted soil and form a drying front when rainfall stopped, causing soil water to migrate upward again [8]. On the other hand, there was a significant contrast in the calculation results of various periods due to the influence of different rainfall intensities. For example, the maximum instantaneous rate of the three periods at 10 cm were -0.037 , -0.222 , and -0.748 cm h^{-1} , respectively. Although rainfall was larger for P3 than for P2, the cumulative infiltration amount at the 50 cm depth in P2 was greater, which was mainly due to the higher soil water content in September of P2 than in April of P3. These quantitative results imply that the established model offers a suitable way to estimate the infiltration rate and amount, which are crucial for clarifying the soil hydrological cycle.

Table 5. Infiltration process of different rainfall periods.

Depth (cm)	P2		P3		P4	
	Maximum Rate (cm h^{-1})	Cumulative Amount (cm)	Maximum Rate (cm h^{-1})	Cumulative Amount (cm)	Maximum Rate (cm h^{-1})	Cumulative Amount (cm)
10	-0.037	0.73	-0.222	1.06	-0.748	4.69
20	-0.016	0.46	-0.076	0.57	-0.546	3.94
50	-0.006	0.20	-0.003	0.11	-0.153	2.34
100	/	/	/	/	-0.025	1.43

4. Discussion

4.1. Influence of Rainfall on Soil Liquid and Vapor Transfer

When rainfall penetrated the vadose zone, soil liquid water and vapor flow were mainly impacted by two factors. As indicated by the simulation results, soil water potential and temperature gradients changed significantly when rainfall occurred, and the variations were closely related to the rainfall intensity. The driving force not only dominated the movement direction of soil liquid and vapor, but also affected the flux density. In addition, the hydraulic conductivity was another factor that affected soil water movement. Since the vapor flux has been confirmed to be mainly driven by temperature gradients, the effect of isothermal hydraulic conductivity for water vapor (K_{vh}) can be ignored, while the isothermal hydraulic conductivity for liquid water (K_{lh}) and thermal hydraulic conductivities for liquid water (K_{lT}) and water vapor (K_{vT}) play critical roles in soil liquid and vapor transfer [48,49]. Because the calculations for K_{lh} and K_{lT} were closely related (Equation (2)), the

variations in these two variables were similar, which were significantly increased (usually three to five orders of magnitude) when rainfall occurred. This significant increase indicated that K_{lh} should be the dominant factor affecting the flux density during the rainfall periods, while the variation in the soil matric potential gradient played a greater role in liquid water flux on dry days. In contrast, K_{vT} decreased in response to rainfall events, which can be attributed to the reduction in pore air content and vapor diffusivity because of the increase in soil water content [31]. Unlike K_{lh} and K_{IT} , it was the reduction in both K_{vT} and the soil temperature gradient that resulted in the decrease in vapor flux [48,50].

During the analyzed period, the total rainfall amount reached 640.2 mm, which far exceeds the local average rainfall. Affected by frequent rainfall events, the isothermal liquid water flux in deep layer varied significantly as well. The calculated cumulative amount at the 200 cm depth was approximately 90 mm, and most of the leakage amount would eventually recharge the groundwater. With the established model, the liquid and vapor transfer in different years with various rainfall amounts can be investigated; these are crucial for guiding agricultural irrigation and rational utilization of water resources in arid areas.

4.2. The Role of Vapor Flux in the Soil Hydrological Cycle

Based on the simulation results, the characteristics of vapor flow during both dry and rainy conditions are described in detail. Since the vapor density in the vadose zone is almost saturated most of the time, water vapor will evaporate or condense accordingly as long as the soil temperature changes [51]. Driven by the temperature gradient, vapor mainly flows downward from the surface towards the deep soil layer in the daytime, while it moves upward at night. The transfer and condensation of water vapor has a significant impact on soil water flow in the upper and lower layers of the vadose zone. For the shallow layer, the vapor flux dominated by the temperature gradient is relatively larger. For instance, the average proportion of the thermal vapor flux in the total water flux accounted for 15.3% at the 2 cm depth of P1, which corresponds with the calculation results of Zhang et al. [33] and Deb et al. [51]. With the increase in dry periods as well as the temperature gradient, the instantaneous proportion could reach nearly 40%, and the flux density would continue to increase. Taking the Gobi Desert of northwestern China as an example, where the annual precipitation is only 35.2 mm, Du et al. [52] found that the quantity of vapor flux exceeds the liquid flux, controlling soil water transfer. The above finding confirms that the impact of vapor flow should not be ignored in arid and semi-arid regions, especially when the soil has a long-term dry condition [32]. Although the vapor flux is relatively lower in deep layers due to the decreased driving force, vapor driven by the temperature gradient continuously migrates and accumulates towards the deep layer, which should not be ignored [53].

In addition to affecting soil water transfer during the unfrozen period, the effect of vapor flow should be significant when soil is frozen [54]. For the Mu Us Sandy Land and similar arid areas in northwestern China, it is noted that these regions belong to seasonally frozen areas. During the freezing period, the soil liquid flux is significantly reduced due to the presence of ice in soil pores, leading to the impact of vapor flow being more significant. The maximum frozen depth usually reached 150 cm in the study area, and vapor mainly flow downward towards the frozen layer with a lower temperature [25]. Therefore, the seasonal vapor transfer during the freezing–thawing period has a significant impact on soil hydrological cycle processes, such as influencing soil moisture distribution and promoting the formation of a higher-water-content layer.

4.3. Study Limitations and Future Research Prospects

Based on field observations and experiments, a coupled water–vapor–heat transport model was established using the Hydrus-1D program in this study. For the shallow soil layer, the fitting accuracy was affected by external environmental factors. While at 100 cm depth, the relatively large discrepancy between the observed and simulated soil water content was likely caused by a sudden change in soil hydraulic properties above and below

80 cm depth due to different soil textures (Tables 1 and 2). By installing more monitoring points in the soil profile and determining soil hydraulic parameters (e.g., the vapor diffusivity in soil and the enhancement factor) using experimental rather than empirical methods, the model's accuracy is expected to be further improved [39,55]. In addition, it is noted that the simulated results were obtained based on in situ measurements at a site with bare land, thus similar results as those obtained could be expected for other areas with similar soil conditions. For areas with other soil conditions or shallow groundwater levels, the established model may be inappropriate and may need to be modified. Nevertheless, the simulation and analyzed results confirmed that the model considering coupled liquid water–vapor–heat transport should be appropriate for evaluating soil water flow in arid areas.

In arid and semi-arid regions, the capacity of soil water storage and rainfall infiltration are of great significance in determining vegetation states [56]. The soil layers at shallow depths are the main layers receiving precipitation and providing a regular water source for vegetation growth. In past studies, research has mainly focused on the impact of liquid water on vegetation growth, while ignoring the effect of water vapor. The condensation and aggregation of vapor in Mu Us Sandy Land has been proven to be crucial for preserving the desert ecosystem, which could provide an important water source for the growth of vegetation such as *Salix psammophila* and *Artemisia ordosica*. The impact of vegetation on soil water is mainly because of its influence on infiltration rates and transpiration, and investigating the response of vegetation to precipitation is a key challenge [57,58]. A root water uptake model can clarify the influence of water uptake on the soil water flow dynamics, and a precise and proper model would be significant for investigating the vegetation water mechanism in arid regions. By coupling the root water uptake process into the coupled water, vapor, and heat transport model, the specific effect of vapor flux on plant growth and the ecological significance of soil water could be clarified in detail in future research, which would be crucial for vegetation restoration in arid areas.

5. Conclusions

To better understand soil liquid and vapor movement and their response to rainfall events in arid and semi-arid areas, the typical Mu Us Sandy Land in northwest China was selected as the study site, and a combination of in situ observations, field and laboratory tests, and numerical simulation methods were adopted. Based on the observed data, a combined water, vapor, and heat transport model was established using the Hydrus-1D software, and the model's accuracy was proved using the in situ observation data. The comparison of the simulation results in different periods indicated that rainfall completely changed the distribution of soil matric potential, temperature, and the driving forces, and the variations were closely correlated with the rainfall intensity. The isothermal liquid flux was the most significant component of the total water flux in the vadose zone, followed by the thermally driven liquid and vapor fluxes. The significance of the vapor flux was demonstrated by the fact that it accounted for roughly 15% of the shallow layer's total water flux in dry conditions, while the vapor flux became negligible during rainy periods. In addition to the driving forces, the significant changes in hydraulic conductivity also contributed to the variation in liquid water and vapor flux.

The findings of this research may shed further light on how the soil water cycle works in the Mu Us Sandy Land, which could provide a theoretical basis to further explore the specific effect of soil water on vegetation growth. By coupling the vegetation module into the coupled water, vapor, and heat transport process, the effect of vapor flux on plant growth and the ecological significance of soil water could be clarified in detail, which will be crucial for vegetation restoration and ecological environment protection in arid areas.

Author Contributions: Conceptualization, T.L. and C.Z.; methodology, T.L. and C.Z.; software and formal analysis, T.L., X.W. and Y.Z.; data curation, J.W., X.W. and Y.Z.; writing—original draft preparation, T.L. and J.W.; writing—review and editing, C.Z., B.Z., X.L. and W.Y.; supervision, C.Z., B.Z. and X.L.; funding acquisition, C.Z. and X.L. All authors have read and agreed to the published version of the manuscript.

Funding: This study was financially supported by the National Natural Science Foundation of China (No. 42202279, 41877179), China Postdoctoral Science Foundation (No. 2022M720536), the Fundamental Research Funds for the Central Universities, CHD (No. 300102292105, 300102292904), and the Scientific Research Program Funded by Shaanxi Provincial Education Department (No. 15JK1284).

Data Availability Statement: The data that support the findings of this study are available from the corresponding author upon reasonable request.

Acknowledgments: The authors are grateful to the editor and reviewers for providing positive and constructive comments for this paper.

Conflicts of Interest: The authors declare no conflict of interest.

Abbreviations

Symbol	Definition
θ_l	Volumetric liquid water content, $\text{m}^3 \text{m}^{-3}$
θ_v	Volumetric water vapor content, $\text{m}^3 \text{m}^{-3}$
θ_r	Residual water content, $\text{m}^3 \text{m}^{-3}$
θ_s	Saturated water content, $\text{m}^3 \text{m}^{-3}$
K_{lh}	Isothermal hydraulic conductivity for liquid water, m s^{-1}
K_{lT}	Thermal hydraulic conductivity for liquid water, $\text{m}^2 \text{K}^{-1} \text{s}^{-1}$
K_{vh}	Isothermal hydraulic conductivity for water vapor, m s^{-1}
K_{vT}	Thermal hydraulic conductivity for water vapor, $\text{m}^2 \text{K}^{-1} \text{s}^{-1}$
C_p	Volumetric heat capacity of moist soil, $\text{J m}^{-3} \text{K}^{-1}$
C_v	Volumetric heat capacity of water vapor, $\text{J m}^{-3} \text{K}^{-1}$
C_w	Volumetric heat capacity of liquid water, $\text{J m}^{-3} \text{K}^{-1}$
ρ_v	Vapor density, kg m^{-3}
ρ_l	Liquid water density, kg m^{-3}
ρ_{sv}	Saturated vapor density, kg m^{-3}
K_s	Saturated hydraulic conductivity, m s^{-1}
q_{lh}	Isothermal liquid water flux, m s^{-1}
q_{lT}	Thermal liquid water flux, m s^{-1}
q_{vh}	Isothermal water vapor flux, m s^{-1}
q_{vT}	Thermal water vapor flux, m s^{-1}
D	Vapor diffusivity in air, $\text{m}^2 \text{s}^{-1}$
g	Gravitational acceleration, m s^{-2}
h	Pressure head, m
L_0	Volumetric latent heat of vaporization of liquid water, J m^{-3}
M	Molecular weight of water, kg mol^{-1}
R	Universal gas constant, $\text{J mol}^{-1} \text{K}^{-1}$
T	Temperature, K
t	Time, s
z	Vertical depth from the surface, m
γ	Surface tension of soil water, J m^{-2}
λ	Soil thermal conductivity, $\text{W m}^{-1} \text{K}^{-1}$

References

- Huang, J.; Zhang, W.; Zuo, J.; Bi, J.; Shi, J.; Wang, X.; Chang, Z.; Huang, Z.; Yang, Z.; Zhang, B.; et al. An overview of the semi-arid climate and environment research observatory over the loess plateau. *Adv. Atmos. Sci.* **2008**, *25*, 906–921. [[CrossRef](#)]
- Feng, S.; Fu, Q. Expansion of global drylands under a warming climate. *Atmos. Chem. Phys.* **2013**, *13*, 10081–10094. [[CrossRef](#)]
- Ravi, S.; Breshears, D.D.; Huxman, T.E.; D’Odorico, P. Land degradation in drylands: Interactions among hydrologic–aeolian erosion and vegetation dynamics. *Geomorphology* **2010**, *116*, 236–245. [[CrossRef](#)]

4. You, Y.; Zhou, N.; Wang, Y. Comparative study of desertification control policies and regulations in representative countries of the Belt and Road Initiative. *Glob. Ecol. Conserv.* **2021**, *27*, e01577. [[CrossRef](#)]
5. Sun, Y.; Zhang, N.; Yan, J.; Zhang, S. Effects of soft rock and biochar applications on Millet (*Setaria italica* L.) crop performance in sandy soil. *Agronomy* **2020**, *10*, 669. [[CrossRef](#)]
6. Xu, Q.; Li, H.; Chen, J.; Cheng, X.; Liu, S.; An, S. Water use patterns of three species in subalpine forest, Southwest China: The deuterium isotope approach. *Ecohydrology* **2011**, *4*, 236–244. [[CrossRef](#)]
7. Schwinning, S.; Sala, O.E. Hierarchy of Responses to Resource Pulses in Arid and Semi-Arid Ecosystems. *Oecologia* **2004**, *141*, 211–220. [[CrossRef](#)]
8. Zeng, Y.; Su, Z.; Wan, L.; Yang, Z.; Zhang, T.; Tian, H.; Shi, X.; Wang, X.H.; Cao, W. Diurnal pattern of the drying front in desert and its application for determining the effective infiltration. *Hydrol. Earth Syst. Sci.* **2009**, *13*, 703–714. [[CrossRef](#)]
9. Yang, L.; Chen, L.; Wei, Z.; Yu, Y.; Zhang, H. Comparison of deep soil moisture in two revegetation watersheds in semi-arid regions. *J. Hydrol.* **2014**, *513*, 314–321. [[CrossRef](#)]
10. Dymond, S.F.; Bradford, J.B.; Bolstad, P.V.; Kolka, R.K.; Sebestyen, S.D.; DeSutter, T.M. Topographic, edaphic, and vegetative controls on plant-available water. *Ecohydrology* **2017**, *10*, e1879. [[CrossRef](#)]
11. Zhao, M.; Wang, W.; Wang, Z.; Chen, L.; Ma, Z.; Wang, Q. Water use of Salix in the variably unsaturated zone of a semiarid desert region based on in-situ observation. *J. Hydrol.* **2020**, *591*, 125579. [[CrossRef](#)]
12. Hayat, M.; Zha, T.; Jia, X.; Iqbal, S.; Qian, D.; Bourque, C.P.; Khan, A.; Tian, Y.; Bai, Y.; Liu, P.; et al. A multiple-temporal scale analysis of biophysical control of sap flow in Salix psammophila growing in a semiarid shrubland ecosystem of northwest China. *Agr. For. Meteorol.* **2020**, *288–289*, 107985. [[CrossRef](#)]
13. Naem, S.; Zhang, Y.; Zhang, X.; Tian, J.; Abbas, S.; Luo, L.; Meresa, H.K. Both climate and socioeconomic drivers contribute in vegetation greening of the Loess Plateau. *Sci. Bull.* **2021**, *66*, 1160–1163. [[CrossRef](#)]
14. Chen, Y.; He, J.; He, Y.; Gao, W.; Zheng, C.; Liu, X. Seasonal hydrological traits in Salix psammophila and its responses to soil moisture and meteorological factors in desert areas. *Ecol. Indic.* **2022**, *136*, 108626. [[CrossRef](#)]
15. Banwart, S.A.; Bernasconi, S.; Bloem, J.; Blum, W.; Brandao, M.; Brantley, S.L.; Chabaux, F.; Duffy, C.; Kram, P.; Lria, G.; et al. Soil processes and functions in critical zone observatories: Hypotheses and experimental design. *Vadose Zone J.* **2011**, *10*, 974–987. [[CrossRef](#)]
16. Nakhaei, M.; Šimůnek, J. Parameter estimation of soil hydraulic and thermal property functions for unsaturated porous media using the HYDRUS-2D code. *J. Hydrol. Hydromech.* **2014**, *62*, 7–15. [[CrossRef](#)]
17. Rubio, E.; Rubio-Alfaro, M.d.S.; Hernández-Marín, M. Wetting front velocity determination in soil infiltration processes: An experimental sensitivity analysis. *Agronomy* **2022**, *12*, 1155. [[CrossRef](#)]
18. Scanlon, B.R.; Keese, K.; Reedy, R.C.; Šimůnek, J.; Andraski, B.J. Variations in flow and transport in thick desert vadose zones in response to paleoclimatic forcing (0–90 kyr): Field measurements, modeling, and uncertainties. *Water Resour. Res.* **2003**, *39*, 1179–1196. [[CrossRef](#)]
19. Cheng, Y.; Zhan, H.; Yang, W. Deep soil water recharge response to precipitation in Mu Us Sandy Land of China. *Water Sci. Eng.* **2018**, *11*, 139–146. [[CrossRef](#)]
20. Kidron, G.J. Dune crests serve as preferential habitats for perennial plants during frequent drought years. *J. Hydrol.* **2015**, *522*, 295–304. [[CrossRef](#)]
21. Wang, X. Vapor flow resistance of dry soil layer to soil water evaporation in arid environment: An overview. *Water* **2015**, *7*, 4552–4574. [[CrossRef](#)]
22. Bao, H.; Koike, T.; Yang, K.; Wang, L.; Shrestha, M.; Lawford, P. Development of an enthalpy-based frozen soil model and its validation in a cold region in China. *J. Geophys. Res.* **2016**, *121*, 5259–5280. [[CrossRef](#)]
23. Rao, P.; Wang, Y.; Liu, Y.; Wang, X.; Hou, Y.; Pan, S.; Wang, F.; Zhu, D. A comparison of multiple methods for mapping groundwater levels in the Mu Us Sandy Land, China. *J. Hydrol. Reg. Stud.* **2022**, *43*, 101189. [[CrossRef](#)]
24. Yu, L.; Zeng, Y.; Su, Z. Understanding the mass, momentum, and energy transfer in the frozen soil with three levels of model complexities. *Hydrol. Earth Syst. Sc.* **2020**, *24*, 4813–4830. [[CrossRef](#)]
25. Zheng, C.; Šimůnek, J.; Zhao, Y.; Lu, Y.; Liu, X.; Shi, C.; Li, H.; Yu, L.; Zeng, Y.; Su, Z. Development of the Hydrus-1D Freezing module and its application in simulating the coupled movement of water, vapor, and heat. *J. Hydrol.* **2021**, *598*, 126250. [[CrossRef](#)]
26. Philip, J.R.; de Vries, D.A. Moisture movement in porous materials under temperature gradient. *Trans. Am. Geophys. Union* **1957**, *38*, 222–232. [[CrossRef](#)]
27. Cass, A.; Campbell, S.; Jones, T.L. Enhancement of thermal water vapor diffusion in soil. *Soil Sci. Soc. Am. J.* **1984**, *48*, 25–32. [[CrossRef](#)]
28. Cahill, A.T.; Parlange, M.B. On water vapor transport in field soils. *Water Resour. Res.* **1998**, *34*, 731–739. [[CrossRef](#)]
29. Novak, M.D. Dynamics of the near-surface evaporation zone and corresponding effects on the surface energy balance of a drying bare soil. *Agr. For. Meteorol.* **2010**, *150*, 1358–1365. [[CrossRef](#)]
30. Banimahd, S.A.; Zand-Parsa, S. Simulation of evaporation, coupled liquid water, water vapor and heat transport through the soil medium. *Agr. Water Manag.* **2013**, *130*, 168–177. [[CrossRef](#)]
31. Bittelli, M.; Ventura, F.; Campbell, G.S.; Snyder, R.L.; Gallegati, F.; Pisa, P.R. Coupling of heat, water vapor, and liquid water fluxes to compute evaporation in bare soils. *J. Hydrol.* **2008**, *362*, 191–205. [[CrossRef](#)]

32. Zhou, H.; Zhao, W. Evolution of soil-water states in the vadose zone of a desert soil after an extreme rainfall event and its impact on the ecosystem. *Hydrogeol. J.* **2021**, *29*, 2127–2147. [[CrossRef](#)]
33. Zhang, M.; Wen, Z.; Xue, K.; Chen, L.; Li, D. A coupled model for liquid water, water vapor and heat transport of saturated–unsaturated soil in cold regions: Model formulation and verification. *Environ. Earth Sci.* **2016**, *75*, 701–719. [[CrossRef](#)]
34. Cheng, D.; Li, Y.; Chen, X.; Wang, W.; Hou, G.; Wang, C. Estimation of groundwater evapotranspiration using diurnal water table fluctuations in the Mu Us Desert, northern China. *J. Hydrol.* **2013**, *490*, 106–113. [[CrossRef](#)]
35. Šimůnek, J.; Šejna, M.; Saito, H.; Sakai, M.; van Genuchten, M.T. *The HYDRUS-1D Software Package for Simulating the One-Dimensional Movement of Water, Heat, and Multiple Solutes in Variably Saturated Media*; Version 4.0; HYDRUS Software Series 3; Department of Environmental Sciences, University of California Riverside: Riverside, CA, USA, 2008.
36. Cheng, Q.; Sun, Y.; Jones, S.B.; Vasilyev, V.I.; Popov, V.V.; Wang, G.; Zheng, L. In situ measured and simulated seasonal freeze-thaw cycle: A 2-year comparative study between layered and homogeneous field soil profiles. *J. Hydrol.* **2014**, *519*, 1466–1473. [[CrossRef](#)]
37. Sun, Y.; Cheng, Q.; Xue, X.Z.; Fu, L.; Chai, J.; Meng, F.; Lammers, P.S.; Jones, S.B. Determining in-situ soil freeze-thaw cycle dynamics using an access tube-based dielectric sensor. *Geoderma* **2012**, *189–190*, 321–327. [[CrossRef](#)]
38. Saito, H.; Šimůnek, J.; Mohanty, B. Numerical analyses of coupled water, vapor, and heat transport in the vadose zone. *Vadose Zone J.* **2006**, *5*, 784–800. [[CrossRef](#)]
39. Sakai, M.; Toride, N.; Šimůnek, J. Water and vapor movement with condensation and evaporation in a sandy column. *Soil Sci. Soc. Am. J.* **2009**, *73*, 707. [[CrossRef](#)]
40. Mualem, Y. A new model for predicting the hydraulic conductivity of unsaturated porous media. *Water Resour. Res.* **1976**, *12*, 513–522. [[CrossRef](#)]
41. van Genuchten, M.T. A closed-form equation for predicting the hydraulic conductivity of unsaturated soils. *Soil Sci. Soc. Am. J.* **1980**, *44*, 892–898. [[CrossRef](#)]
42. Šimůnek, J.; van Genuchten, M.T.; Šejna, M. HYDRUS: Model use, calibration, and validation. *Trans. ASABE* **2012**, *55*, 1261–1274. [[CrossRef](#)]
43. Chung, S.O.; Horton, R. Soil heat and water flow with a partial surface mulch. *Water Resour. Res.* **1987**, *23*, 2175–2186. [[CrossRef](#)]
44. Šimůnek, J.; van Genuchten, M.T.; Šejna, M. Development and applications of the HYDRUS and STANMOD software packages and related codes. *Vadose Zone J.* **2008**, *7*, 587–600. [[CrossRef](#)]
45. Moghbel, F.; Mosaedi, A.; Aguilar, J.; Ghahraman, B.; Ansari, H.; Gonçalves, M.C. Uncertainty analysis of HYDRUS-1D model to simulate soil salinity dynamics under saline irrigation water conditions using Markov Chain Monte Carlo algorithm. *Agronomy* **2022**, *12*, 2793. [[CrossRef](#)]
46. Dahiya, R.; Ingwersen, J.; Streck, T. The effect of mulching and tillage on the water and temperature regimes of a loess soil: Experimental findings and modeling. *Soil Tillage Res.* **2007**, *96*, 52–63. [[CrossRef](#)]
47. Kroener, E.; Vallati, A.; Bittelli, M. Numerical simulation of coupled heat, liquid water and water vapor in soils for heat dissipation of underground electrical power cables. *Appl. Therm. Eng.* **2014**, *70*, 510–523. [[CrossRef](#)]
48. Huang, J.; Hou, R.; Yang, H. Diurnal pattern of liquid water and water vapor movement affected by rainfall in a desert soil with a high water table. *Environ. Earth Sci.* **2015**, *75*, 73–88. [[CrossRef](#)]
49. Gao, W.; Liu, X.; Zheng, C.; Lu, Y.; He, J.; He, Y. Comparison of the soil water, vapor, and heat dynamics between summer maize and bare fields in arid and semi-arid areas. *Agronomy* **2023**, *13*, 1171. [[CrossRef](#)]
50. Zeng, Y.; Wan, L.; Su, Z.; Saito, H.; Huang, K.; Wang, X. Diurnal soil water dynamics in the shallow vadose zone (field site of China University of Geosciences, China). *Environ. Geol.* **2008**, *58*, 11–23. [[CrossRef](#)]
51. Deb, S.K.; Shukla, M.K.; Sharma, P.; Mexal, J.G. Coupled liquid water, water vapor, and heat transport simulations in an unsaturated zone of a sandy loam field. *Soil Sci.* **2011**, *176*, 387–398. [[CrossRef](#)]
52. Du, C.; Yu, J.; Wang, P.; Zhang, Y. Analysing the mechanisms of soil water and vapour transport in the desert vadose zone of the extremely arid region of northern China. *J. Hydrol.* **2017**, *558*, 592–606. [[CrossRef](#)]
53. Xiang, L.; Yu, Z.; Chen, L.; Mon, J.; Lu, H. Evaluating coupled water, vapor, and heat flows and their influence on moisture dynamics in arid regions. *J. Hydrol. Eng.* **2012**, *17*, 565–577. [[CrossRef](#)]
54. Hou, B.; Jin, H.; Flerchinger, G.; Lv, J.; He, H. Canopy effect: Water vapor transmission in froze soils with impermeable surface. *Acta Geotech.* **2023**. [[CrossRef](#)]
55. Gao, H.; Shao, M. Effects of temperature changes on soil hydraulic properties. *Soil Till. Res.* **2015**, *153*, 145–154. [[CrossRef](#)]
56. Wang, S.; Fu, B.; Gao, G.; Yao, X.; Zhou, J. Responses of soil moisture in different land cover types to rainfall events in a re-vegetation catchment area of the Loess Plateau, China. *Catena* **2013**, *101*, 122–128. [[CrossRef](#)]
57. Zhao, M.; Wang, W.; Ma, Z.; Wang, Q.; Wang, Z.; Chen, L.; Fu, B. Soil water dynamics based on a contrastive experiment between vegetated and non-vegetated sites in a semiarid region in Northwest China. *J. Hydrol.* **2021**, *603*, 126880. [[CrossRef](#)]
58. Bi, Y.; Xie, L.; Wang, Z.; Wang, K.; Liu, W.; Xie, W. Arbuscular mycorrhizal symbiosis facilitates apricot seedling (*Prunus sibirica* L.) growth and photosynthesis in northwest China. *Int. J. Coal Sci. Technol.* **2021**, *8*, 473–482. [[CrossRef](#)]

Disclaimer/Publisher’s Note: The statements, opinions and data contained in all publications are solely those of the individual author(s) and contributor(s) and not of MDPI and/or the editor(s). MDPI and/or the editor(s) disclaim responsibility for any injury to people or property resulting from any ideas, methods, instructions or products referred to in the content.